Multi-Paralleled LCC Reactive Power Compensation Networks and Their Tuning Method for Electric Vehicle Dynamic Wireless Charging

Shijie Zhou and Chunting Chris Mi, *Fellow, IEEE*

***Abstract*—Dynamic wireless power transfer (WPT) is a practical method to solve electric vehicle (EV) range anxiety and reduce the cost of on-board batteries. This paper presents a novel dynamic WPT system that combines the advantages of pads array and segmental long coils coupler. In the proposed circuit, several paralleled LCC reactive power compensation networks (RPCNs) in the primary side were excited by a sole inverter and the power distribution was realized automatically; an auxiliary LCC network was proposed to regulate current in the primary coil to minimize the electromagnetic interference (EMI) and reduce the system's power loss. A scaled-down prototype of a dynamic wireless charging system was developed to prove the validity of the theoretical analysis.**

***Index Terms*—Current regulation, dynamic charging, LCC reactive power compensation network (RPCN), power distribution, wireless power transfer (WPT).**

I. Introduction

ELECTRIFICATION in the transportation sector has been strongly emphasized for the last several decades due to tougher regulations triggered by environmental concerns and energy security concerns [1]. For electric vehicles (EVs), a high power and large capacity battery pack is equipped as an energy storage unit to make an EV operate for a satisfactory distance, which increases the cost of EV and create range anxiety for EV owners [2]–[4].

To mitigate the cost and range issues, wireless power transfer (WPT) for EV charging has been extensively studied and has begun to commercialize in the last decade. Many topologies have been proposed. Among these, dynamic wireless charging promises to increase vehicle mileage and decrease battery size [5], [6]. The charging occurs while the vehicles are moving over charging tracks or pads, which are installed under the road surface in urban or highway environments. By using dynamic charging, journey idle time due to stops for charging decreases and the ratio of distance over battery size increases [7], so smaller battery packs could be feasible thanks to WPT.

There are mainly two major kinds of primary magnetic couplers in dynamic charging. The first one is a long track coupler, as shown in Fig. 1(a). When an EV with a pickup coil is running along the track, continuous power can be transferred. References [8]–[11] performed analysis and are of great reference value in this area. However, the problem with the track design is that the pickup coil covers only a small portion of the track, which makes the coupling coefficient very small. The poor coupling produces low efficiency and electromagnetic interference (EMI) issues. To solve these issues, references [12] and [13] proposed segmental long tracks, where the track is made of segments with a single power converter and a set of switches to select which segmental track should be excited. The excitation of each segment can be controlled by the switches' ON–OFF state. The electromagnetic field above the inactive segments is significantly reduced. However, complex detection and control circuits such as position sensors and segmental coil switching control circuits are needed in this coupler, which greatly increases the complexities of the control system. The second type of primary magnetic coupler is pads array, as shown in Fig. 1(b) [14]–[16]. In this structure, each pad can be driven by an independent power converter. Thus, the primary pads can be selectively excited without a high-frequency common current in the long track coupler. Moreover, the energized primary pad is covered by the vehicle, meaning the electromagnetic field is shielded so as to have a minimum impact on the surrounding environment. Hence, the efficiency and EMI performance could be as good as that in a stationary charging. However, this mode also requires a position detection circuit to control coil switching. The control process and system response speed should be much faster than the speed of the EV. In addition, the cost to build a power converter for each pad is unaffordable. To solve these problems, a double-coupled method was proposed in [17] and a reflexive field containment idea was proposed in [18].

Both of these methods realized primary pads switching automatically; however, the constant high-frequency current constantly circulating in the intermediary coupler lowers the efficiency in [17]; and the reflexive field containment method exacerbated the phenomenon of power null, which causes

Manuscript received June 20, 2015; revised October 2, 2015; accepted November 18, 2015. Date of publication December 24, 2015; date of current version September 9, 2016.

S. Zhou is with the Department of Electrical and Computer Engineering, University of Michigan, Dearborn, MI 48126 USA (e-mail: Zhoupennstate@gmail.com).

C. C. Mi is with the Department of Electrical and Computer Engineering, San Diego State University, San Diego, CA 92182 USA (e-mail: mi@ieee.org).

Color versions of one or more of the figures in this paper are available online at http://ieeexplore.ieee.org.

Digital Object Identifier 10.1109/TIE.2015.2512236

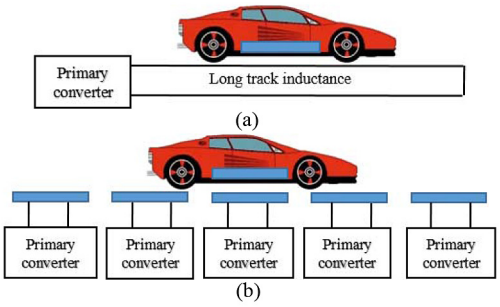

Fig. 1. Two kinds of primary magnetic couplers in a dynamic WPT system. (a) Long track couplers. (b) Segmental couplers.

the output power fluctuations, resulting in only 30% effective charging time [18].

Based on the above analysis, a well-designed dynamic WPT system should be easy to control, highly efficient, low in radiation, relatively stable output power, and affordable. In this paper, a novel dynamic WPT charging scheme in the primary side and the corresponding control method is proposed. The proposed system combines the aforementioned advantages of the two kinds of couplers. In the proposed scheme, several paralleled reactive power compensation networks (RPCNs) are adopted to compose the energy transmitting pads array in the primary side. These RPCNs are excited by a single primary converter, which is quite cost-effective. The excited current flowing into every RPCN could be automatically built up when the pickup coil is coupled or partly coupled. A DDQ coil in the pickup side is used to eliminate the power null phenomenon. Given constant current in the primary coil in the RPCN, a novel current regulation circuit and its corresponding control method are proposed to regulate the primary current in every primary coil in the pads array to lower EMI and improve system efficiency.

The following assumptions are made throughout this paper: 1) the gap between every two adjacent primary coils is small enough that it can be neglected; 2) the input impedance of the pickup side is always purely resistive; and 3) the equivalent impedance of the battery does not change as the EV passes through one primary coil.

II. LCC Network for the Dynamic WPT System

A. Fundamentals of WPT System

A typical WPT system comprises three main parts: 1) a primary power converter; 2) magnetic coupling with primary and pickup RPCNs; and 3) a pickup ac–dc converter [16], as shown in Fig. 2. A high-frequency sinusoidal current is produced by an ac–dc–ac converter in the primary side, usually ranging from 80 to 90 kHz for EV charging, flowing into the one or several primary RPCNs and exciting primary pads, which create a high flux density in the vicinity of the primary coil. The impedance of RPCNs in the primary and pickup side is matched to the impedances of primary pad inductance L_1 and the pickup coil inductance L_s, respectively, at the resonant frequency. The high-frequency current induced by L_s and compensated by the pickup RPCN is then rectified and transformed into usable charging voltage for the battery [17].

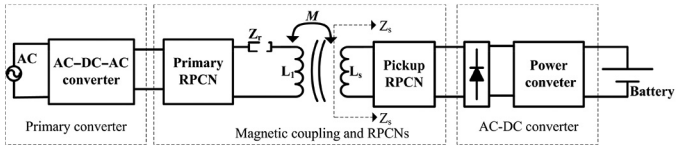

Fig. 2. Typical structure of WPT system.

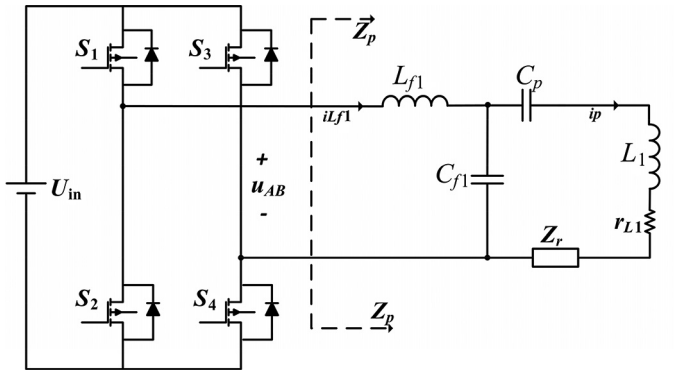

Fig. 3. LCC compensation network in the primary side.

In Fig. 2, M is the mutual inductance between the primary and pickup coils; Z_s is the input impedance of the pickup side. The reflected impedance Z_r is indicated by the dashed line and solved as

$$Z_r = (\omega^2 M^2)/Z_s \tag{1}$$

where ω is the system operation frequency. By assumptions, Z_s is a constant pure resistance. Therefore, M is the only variable that could influence the output power as long as the parameters in the WPT system are properly designed.

B. LCC RPCN in the Primary Side

The LCL RPCN, which is widely used in inductive heating and early WPT systems, performs as a current source at resonance frequency [21], [22]. To cancel the nonlinear effect of the rectifier diodes in the pickup side, another capacitor is introduced to form an LCC network, which could achieve an exact unit power factor under a predetermined load condition [4]. A typical LCC topology in the primary is shown in Fig. 3. A voltage-fed, full-bridge converter is composed by MOSFETs S_1–S_4. C_{f1} is the compensating capacitor for freewheeling inductance L_{f1}; C_p partly compensates primary coil L_1; r_{L1} is the resistance of L_1; Z_p is the output impedance of the inverter; U_{in} is the input dc voltage; u_{AB} and i_{Lf1} are the output voltage and current of the inverter, respectively; i_p is high-frequency current in the primary coil.

For the first step, a concise characteristic of the proposed compensation network will be given by analyzing the first-order harmonics of the square voltage waveform at the switching frequency [23]. The resistance on all the capacitors is neglected for simplicity. The circuit parameters are designed by the following equations to achieve a constant resonant frequency for the topology

$$\begin{cases} L_{f1}C_{f1} = 1/\omega_0^2 \\ (L_1 - L_{f1})\, C_p = 1/\omega_0^2 \end{cases} \tag{2}$$

where ω_0 is the angular constant resonant frequency. Based on the impedance analysis, the $Z_p - \omega$ function can be written as

$$Z_p(\omega) = \frac{1}{\frac{1}{Z_r + r_{L1} + j\omega L_1 + \frac{1}{j\omega C_p}} + j\omega C_{f1}} + \mathrm{j}\omega L_{f1}. \quad (3)$$

When the system operates at a constant resonant frequency, substitute (2) into (3) and simplify the result as

$$Z_p(\omega_0) = \frac{L_{f1}}{C_{f1}(Z_r + r_{L1})}. \quad (4)$$

From (1) and (4), i_{Lf1} and P_{in}, the input current and input power of the primary RPCN, can be easily solved as

$$i_{Lf1} = u_{AB} C_{f1} \left(\omega^2 M^2 + r_{L1} Z_s\right) / Z_s L_{f1} \quad (5)$$

$$P_{\text{in}} = u_{AB}^2 C_{f1} \left(\omega^2 M^2 + r_{L1} Z_s\right) / Z_s L_{f1}. \quad (6)$$

Both the full-bridge voltage-fed inverter and the LCC compensation network are supposed to operate at steady state and the values of u_{AB}, r_{L1}, C_{f1}, L_{f1}, and Z_s are constant. From (6), the sole variable that could influence output power P_{in} is M and they are positively correlated. In the processing of dynamic charging, M and P_{in} will reach maximum values simultaneously when the primary coil and the pickup coil are in perfect alignment. As the EV moves away, M will gradually reduce to zero and P_{in} will decrease to a minimum value. That means the input power injected into the primary LCC network could be regulated automatically through the change of M as the pickup coil moves away. No auxiliary position detection circuit or segmental coil switching control strategy is needed during the power transfer process. The characteristic of such an LCC topology greatly simplifies the control complexity in the primary side.

The root mean square (rms) of the high-frequency current in the primary coil i_p could also be solved as

$$i_p = u_{AB}/\omega L_{f1}. \quad (7)$$

Equation (7) shows that the sinusoidal current flowing in the primary coil is dependent only on the inverter input voltage regardless of the load and coupling variations. Such constant current can induce significant losses in the primary side coils and result in EMI. This is undesirable for the performance of the LCC-based dynamic charging system. Such phenomenon and the corresponding current regulation control strategy will be discussed in Sections III and IV.

III. Multi-LCC Networks With DDQ Coils

A. Problems and the Proposed Approach

As analyzed in Section II, M is the sole variable that could influence P_{in} and there is a positive correlation between these two parameters. If several LCC networks are paralleled and excited by a single inverter, the input power would be automatically distributed among several sub-LCC networks depending only on the values of M between the primary coil in each network and the pickup coil.

Furthermore, power null is another issue that should be considered. In the dynamic WPT charging system, the output power could be zero at certain positions if closed coils are deployed. The reason is that equal and opposite magnetic field generated by two adjacent primary coils will offset each other at the pickup coil at some particular points. Such phenomenon is labeled as power null which not only results in unstable output voltage but also reduces the effective charging time.

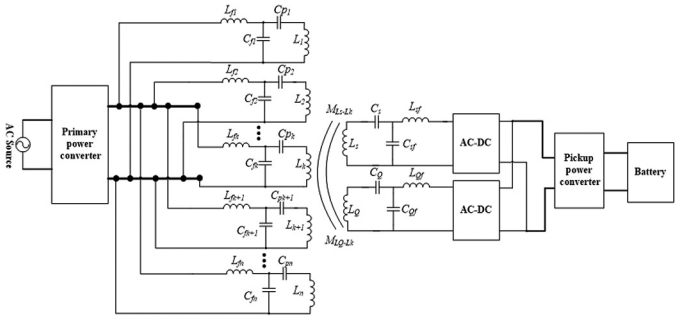

Fig. 4. Multi-LCC networks for the dynamic WPT system.

The DDQ coil structure proposed in [21] eliminates the power pull phenomenon. In this paper, the DDQ coil structure is adopted to avoid the power null with double-LCC compensation networks as shown in Fig. 4. In the proposed circuit, the primary pad array is composed by several DD coils of the same size and self-inductance value. These coils are marked from L_1 to L_n. Correspondingly, the self-inductance values of L_{f1} to L_{fn} are exactly the same. The value of C_{f1} to C_{fn} and C_p to C_n are solved via (2). In the pickup side, DDQ is adopted to eliminate output power null points and maximize energy transmission capability. L_s and L_Q are DD and Q coils, respectively; C_S and C_Q are their compensating capacitors. L_{sf} and L_{Qf} are freewheeling inductors in their own LLC networks, respectively; and C_{sf} and C_{Qf} are compensating capacitors. Parameters in the pickup side are solved by (8)

$$\begin{cases} L_{sf} C_{sf} = 1/\omega_0^2 \\ (L_s - L_{sf}) C_s = 1/\omega_0^2 \\ L_{Qf} C_{Qf} = 1/\omega_0^2 \\ (L_Q - L_{Qf}) C_Q = 1/\omega_0^2 \end{cases}. \quad (8)$$

The coil structure and parameters are shown in Fig. 5. In Fig. 5(a), two duplicate rectangular coils with the same size and turns are in series and placed closely to compose each DD coil in the primary side. Several such DD coils are placed side by side to compose the primary pads array. L_{k-1}, L_k, L_{k+1}, and L_{k+2} are four adjacent DD coils in the primary pad array; subscripts R and L will be used to represent the right half and left half of the DD coil, respectively. The currents in the adjacent rectangular coils must be of opposite directions. In Fig. 5(b), two duplicate rectangular coils compose a pickup DD coil that is identical to the primary coil. The additional rectangular Q coil is overlapped on the center of the DD coil. To maximize power transfer capability, the Q coil is exactly half the size of the DD coil [21].

B. State Analysis

Five reference points are selected to analyze the system's operating conditions, representing an EV moving from one pad

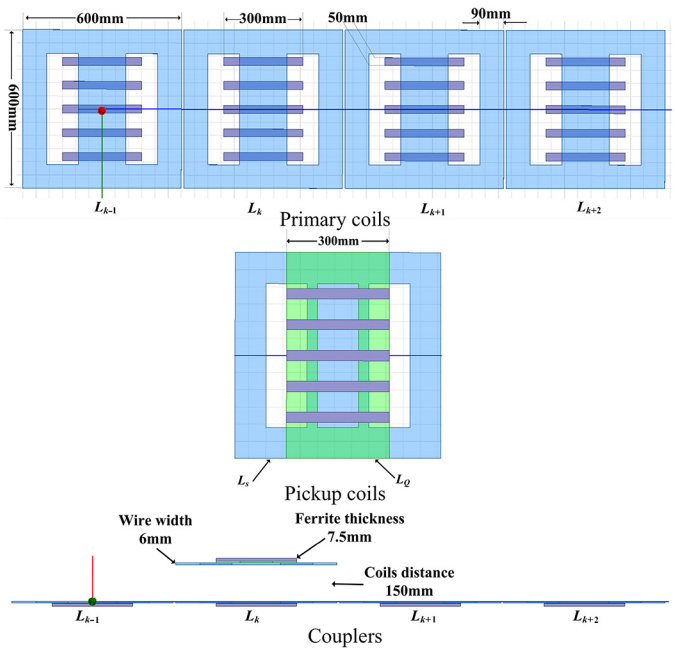

Fig. 5. Couplers structure.

TABLE I
PARAMETERS IN MULTI-LCC CIRCUIT

Parameters	Values	Parameters	Values
U_{in}	320 V	f	85 kHz
L_{fk-1}, L_{fk}, L_{fk+1}, and L_{fk+2}	60 uH	L_s	332.1 uH
C_{fk-1}, C_{fk}, C_{fk+1}, and C_{fk+2}	58.432 nF	L_Q	137 uH
L_{k-1}, L_k, L_{k+1}, andL_{k+2}	332.1 uH	C_s	12.89 nF
C_{pk-1}, C_{pk}, C_{pk+1}, and C_{pk+2}	12.89 nF	C_Q	45.53 nF
r_{Lk-1}, r_{Lk}, r_{Lk+1}, and r_{Lk+2}	0.06 ohm	L_{sf} and L_{Qf}	60 uH
C_{sf} and C_{Qf}	58.432 nF	R	13.3 ohm

TABLE II
MUTUAL INDUCTANCE VALUES IN DIFFERENT STAGES

Parameters	Point1	Point2	Point3	Point4	Point5
$M_{Ls-Lk-1}$(uH)	10.8	–	3.7	–	0.13
$M_{LQ-Lk-1}$(uH)	–	2.43	–	0	–
M_{Ls-Lk} (uH)	90.33	–	42.5	–	9.8
M_{LQ-Lk}(uH)	–	37.33	–	2.43	–
$M_{Ls-Lk+1}$(uH)	9.7	–	43.1	–	92.98
$M_{LQ-Lk+1}$(uH)	–	2.46	–	37.33	–
$M_{Ls-Lk+2}$(uH)	0.13	–	3.7	–	10.7
$M_{LQ-Lk+2}$(uH)	–	0.21	–	2.43	–

to the adjacent one. ANS YS Maxwell electromagnetic simulation software is used to calculate different mutual inductance values at different reference points. The magnetic simulation results and circuit parameters are shown in Tables I and II.

In Fig. 6, four identical DD coils L_{k-1}, L_k, L_{k+1}, and L_{k+2} compose the primary pads array. In the pickup side, subscripts L and R are the left-half and right-half of DD coils both available for primary coils and pickup coil. The solid line circles in the

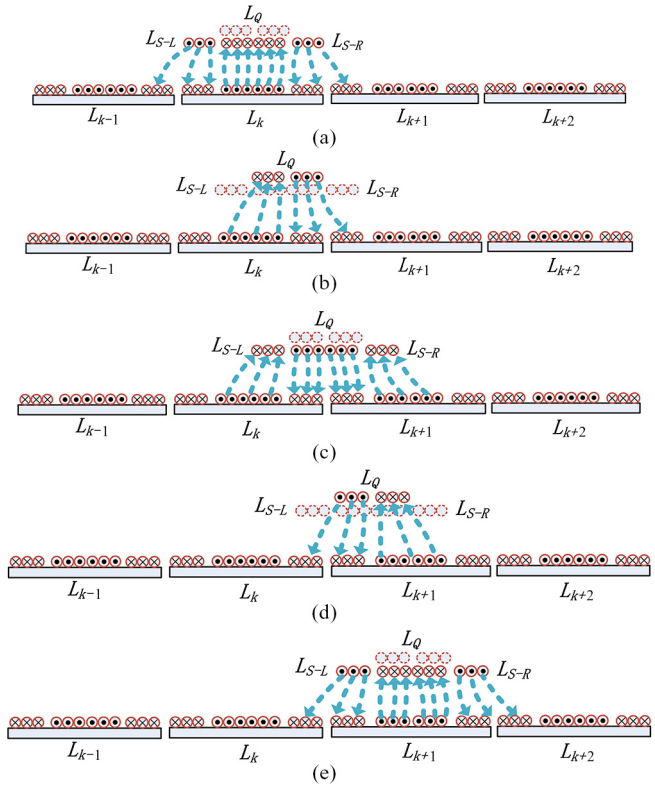

Fig. 6. Coils coupling diagram. (a) Reference point I. (b) Reference point II. (c) Reference point III. (d) Reference point IV. (e) Reference point V.

pickup side indicate that the pickup coils are receiving energy from the primary side and the dashed circles mean the coils are placed at the power null position. The dashed lines are magnetic flux, the density of magnetic flux indicating the level of power transmitted. i_{Lfk-1}, i_{Lfk}, i_{Lfk+1}, and i_{Lfk+2} are input currents of their corresponding RPCNs. Here, a detailed analysis of each point is presented.

Point 1: In Fig. 6(a), L_s is aligned with primary pad coil L_k. M_{Ls-Lk} is much larger than $M_{Ls-Lk-1}$ and $M_{Ls-Lk+1}$, $M_{Ls-Lk+2}$ is nearly zero. According to (5), i_{Lfk} should be much larger than that of the other three. i_{Lfk-1} and i_{Lfk+1} should be equal in theory; i_{Lfk+2} should be zero. L_Q is located at the power null position. The circuit simulation results are shown in Fig. 7(a). In Fig. 7(a), the rms value of i_{Lfk} is much larger than that of i_{Lfk-1} and i_{Lfk+1}, which are almost coincide with each other; i_{Lfk+2} is almost zero. Among the four primary coil currents, only i_{pk-1} is selected to observe the variation of each primary coil current with different coupling coefficients. The amplitude of u_{ab}, which is defined as the common input voltage of the inverter, is scaled down 10 times in all the curves in Fig. 7 for higher resolution.

Point 2: The EV keeps moving along the primary pads array until the L_Q and L_{k-R} are in alignment, as shown in Fig. 6(b). From Table II, M_{LQ-Lk} is much larger than $M_{LQ-Lk-1}$, $M_{LQ-Lk+1}$, and $M_{LQ-Lk+2}$, most input power flows into the kth LCC network rather than other networks. L_s is located on a power null point. However, M_{LQ-Lk} in point 2 is much smaller than M_{Ls-Lk} in point 1 because of coils' size difference, the input power will decrease rapidly. The circuit simulation results are shown in Fig. 7(b) where i_{Lfk} in *point 2* is much smaller

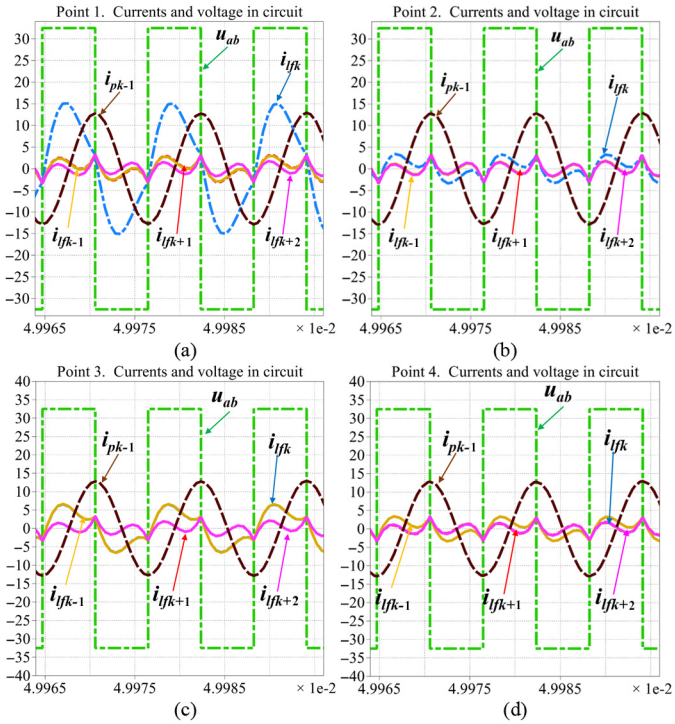

Fig. 7. Circuit simulation results and current curves. (a) Current and voltage in Point 1. (b) Current and voltage in Point 2. (c) Current and voltage in Point 3. (d) Current and voltage in Point 4.

than that in *point 1*; i_{Lfk-1}, i_{Lfk+1}, and i_{Lfk+2} drop to almost zero. Despite the significant change of i_{Lk-1} and P_{in} from point 1 to point 2, the amplitude and phase of i_{pk-1} keeps constant.

Point 3: In Fig. 6(c), L_s couples with both L_k and L_{k+1} when the EV moves to the center of them. L_{k-R} and L_{s-L}, L_{k+1-L}, and L_{s-R} are aligned at this point. The values of M_{Ls-Lk} and $M_{Ls-Lk+1}$ are equal and the input power should be equally shared automatically between these two subcompensation networks. L_Q is located at power null position. The circuit simulation results are shown in Fig. 7(c), i_{Lfk} and i_{Lfk+1} perfectly coincide, i_{Lfk-1} and i_{Lfk+2} are almost down to zero. The amplitude and phase of i_{pk-1} is almost the same as those of the previous points.

Point 4: In Fig. 6(d), the EV keeps moving until the Q coil and L_{k+1-R} are in alignment, L_s is located at a power null point again. The input power mostly injects the $(k+1)$th LCC network rather than other networks. The circuit simulation results are shown in Fig. 7(d), where i_{Lfk+1} in point 4 is much smaller than the sum of i_{Lfk+1} and i_{Lfk} in *point 3*; i_{Lfk}, i_{Lfk-1}, and i_{Lfk+2} are almost zero. i_{pk-1} remains unchanged.

Point 5: L_s and L_{k+1} are aligned, which is shown in Fig. 6(e). Similar to *point 1*, most input power flows into the $(k+1)$th network rather than other networks. L_Q is located at power null position. The circuit simulation results show that the current waveforms resemble those of Fig. 7(a).

From *point 1* to *point 5*, the system goes through a power cycle. During this cycle, most of the input power transfers from one LCC network to the adjacent one gradually and automatically depending only on mutual inductance values between the pickup coil and the various primary coils.

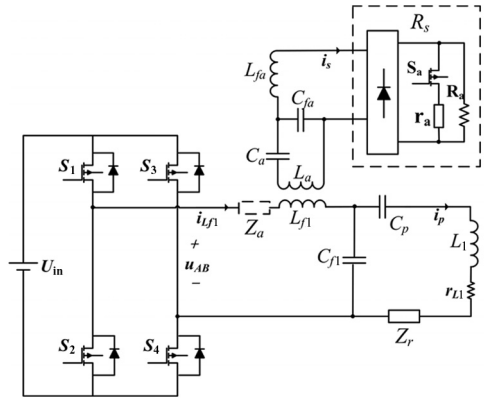

Fig. 8. Primary coil current regulation circuit.

The higher the mutual inductance value, the more power flows into the system. According to circuit simulation results in Fig. 7, the multi-LCC dynamic WPT system has realized power distribution automatically among paralleled compensation networks, which are excited by a single inverter. No additional segmental coil switching control strategy or position tracking detection circuits are needed during the power distribution process, as long as the system operates at the resonant frequency. Soft-switching is realized during the whole power period regardless of coupling variations. Power null points were eliminated via the DDQ coil structure. However, as shown in Fig. 7, the value of i_{pk-1} remains constant irrespective of the coupling change. The simulation results verified (7) that primary coil current in the LCC RPCN is a constant. This characteristic is not expected in the dynamic WPT charging system because the high-frequency constant current in each primary coil not only leads to higher losses and lower efficiency but also results in EMI issues. To overcome this issue, a novel primary coil current regulation circuit and its control method are proposed and analyzed in Section IV.

IV. Primary Coil Current Regulation

A. Current Regulation Circuit

An output power control method called short-circuit decoupling in the pickup side was proposed in [24]. The essence of this control method is changing the value of the reflected load, including real and imaginary parts, to regulate the output power. Inspired by this idea, an auxiliary LCC compensation network is adopted to regulate the rms of the primary coil current, the circuit structure as shown in Fig. 8.

In Fig. 8, C_a and C_{fa} are compensation capacitors for primary coil L_a and freewheeling inductor L_{fa}, respectively, in an auxiliary LCC network; the values of the inductors and capacitors satisfy

$$\begin{cases} L_{fa}C_{fa} = 1/\omega_0^2 \\ (L_a - L_{fa})\,C_{fa} = 1/\omega_0^2 \end{cases} \tag{9}$$

where ω_0 is the reflected impedance from the auxiliary LCC network, which is shown by the dashed line in Fig. 8. R_a is a high resistance, which ranges from 10 k to 100 k ohm; r_a is the turn-ON resistance of MOSFET S_a. The output impedance of

the auxiliary LCC network is R_s, which comprised R_a, r_a, and the internal resistance of the rectifier bridge, whose value can be changed through the use of different control modes. When the system operates at constant resonant frequency, Z_a can be solved

$$Z_a = \omega^2 M_{La-Lf1}^2 C_{fa} R_s / L_{fa} \tag{10}$$

where M_{La-Lf1} is the mutual inductance between L_a and L_{f1}. Unlike the loosely coupling condition between the primary coil and the pickup coil, L_a and L_{f1} are closely coupled, the coupling coefficient usually ranges from 0.75 to 0.9. Primary coil current i_p in Fig. 8 could be solved as

$$i_p = -j \frac{u_{ab} L_{fa}^2 L_{f1} \omega}{\omega^2 L_{f1}^2 L_{fa}^2 + M_{La-Lf1}^2 R_s (Z_r + r_{L1})}. \tag{11}$$

In (11), R_s and L_{fa} are the only two variables whose values need to be optimized by the designer. There are two operation modes in the auxiliary LCC network: 1) short-circuit and 2) open-circuit modes.

When the pickup coil is coupled or partly coupled with the primary coil, Z_r is much larger than r_{L1}, energy is transferred wirelessly from the primary side to the pickup side.

From (11), the minimum value of R_s is expected to maximize i_p and output power. At this time, switch S_a is closed and the auxiliary LCC network operates in short-circuit mode.

Z_r will decrease to zero rapidly when the EV pulls away. Under this condition, the high-resistance value of R_s is expected to limit the amplitude of i_p to reduce coil loss and EMI. At this time, switch S_a is opened and the auxiliary LCC network operates in open-circuit mode. The current passing through R_s can be solved as

$$i_s = -j \frac{L_{fa} M_{La-Lf1} u_{AB} (Z_r + r_{L1})}{\omega^2 L_{fa}^2 L_{f1}^2 + M_{La-Lf1}^2 R_s (Z_r + r_{L1})} \tag{12}$$

where L_{fa} is the other important parameter that needs to be carefully designed. From (11), a smaller L_{fa} is better for limiting the amplitude of i_p when the primary coil and pickup coil are decoupled; however, according to (12), once the primary coil and pickup coil are coupled, a smaller L_{fa} will induce a larger current flowing through switch S_a and burn it down. The relationships between i_p, i_{sa} and L_{fa}, R_s are shown in Fig. 9.

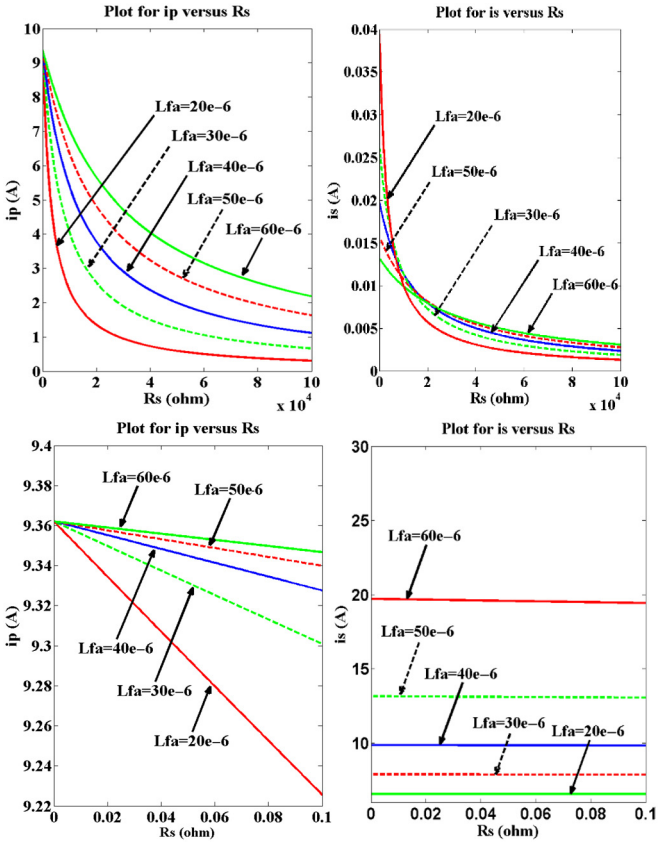

Fig. 9. Relationships between i_p, i_{sa} and L_{fa}, R_s.

B. Current Regulation Control Method

In Fig. 9, $L_a = 60$ uH and $Z_{\text{rmax}} = 30$ ohm, and the values of other circuit parameters are identity in Table I. In Fig. 9, five different L_{fa} values are selected to compare their influence on i_p and i_s in both open- and short-circuit modes. When the pickup coil and primary coils are decoupled, $Z_{\text{rmin}} = 0$ and the auxiliary LCC network work in open-circuit mode. In this mode, when $R_s > 20$k, the smaller value of L_{fa} is more effective for limiting primary coil current i_p, which is shown in Fig. 9(a). Meanwhile, Fig. 9(b) indicates that the value of i_s does not change obviously with L_{fa} and its amplitude is so small that the power loss on R_s could be ignored. When the pickup coil and primary coil are in alignment, $Z_{\text{rmax}} = 30$ ohm and the auxiliary LCC network operates in short circuit mode. In this mode, when $R_s < 0.06$ ohm, i_p does not change obviously with L_{fa}, the results are shown in Fig. 9(c). However, a larger L_{fa} produces a larger amplitude of i_s, as shown in Fig. 9(d).

According to the above analysis, i_p could be regulated via controlling the ON–OFF of S_a in the auxiliary LCC network and there is almost no extra loss during the current regulation process. However, the next question is how to control S_a. In this part, i_{cfa}, the current flowing through C_{fa}, is selected as the reference variable to control the ON–OFF of S_a. The equation of i_{cfa} is calculated as

$$i_{cfa} = \frac{u_{AB} M_{La-Lf1} (Z_r + r_{L1}) (R_s + j\omega L_{fa})}{\omega M_{La-Lf1}^2 R_s (Z_r + r_{L1}) + \omega^3 L_f^2 L_{fa}^2}. \tag{13}$$

Both Z_r and R_s are included in (13). Compared to currents in other components, i_{cfa} is more sensitive to the variations of Z_r and R_s. This brings two benefits. 1) Z_r represents the coupling condition between the primary coil and the pickup coil; therefore, i_{cfa} reflects the change of the EV's position. 2) i_{cfa} has large variations as R_s changes when controlling the primary current. These two benefits justify the reasonableness of employing i_{cfa} as the reference control variable. The simulation results of the control process are shown in Fig. 10.

In Fig. 10, the upper part is the waveform of i_{cfa}, the middle one is the variation of reflected impedance Z_r on a single RPCN's primary side, and the lower one is the waveform of primary coil current i_p. The variations of i_{cfa}, i_p, and Z_r

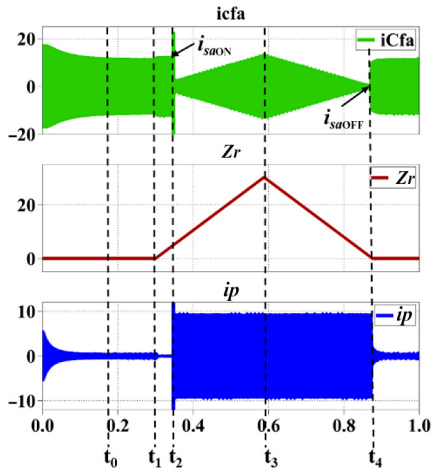

Fig. 10. Simulation of control process.

are simulated for 1 s, representing the process of EV passing through one primary coil. From t_0 to t_1, the primary coil and pickup coil were decoupled and Z_r was almost zero. The auxiliary LCC RPCN was operated in open-circuit mode and i_p was limited. From t_1 to t_2, with the increase in M, i_{cfa} increased gradually. A comparator was introduced to compare the value of i_{cfa} with a reference current i_{saon} and a high-level control signal was sent to close S_a as soon as i_{cfa} exceeds i_{saon} (corresponding to $Z_r = 5$ ohm in the figure).

After S_a was closed, the auxiliary LCC RPCN switches to short-circuit mode. From (11) and (13), i_{cfa} decreases immediately and i_p increases to its maximum value. Then, with M increasing continuously, the two coils came in perfect alignment at point t_3. Z_r, i_{cfa}, M, and the output power achieved their maximum values simultaneously. From t_3 to t_4, with M decreasing, the comparator sent a low-level control signal to open S_a as soon as i_{cfa} is less than a lower reference i_{saoff} (corresponding to $Z_r = 0.5$ ohm in the figure) at t_4. After S_a is opened, the auxiliary LCC RPCN switches to open-circuit mode, where i_{cfa} increases immediately and i_p is limited. At this point, the primary coil has finished its power transfer process.

The essence of this control scheme is comparing i_{cfa} with two reference threshold currents to control the ON–OFF of S_a. A Schmitt trigger, the hysteresis comparator or a digital comparator could realize such control. Compared to position detection control for segmental coils with multiple inverters, this control scheme is not only easy to realize but also truly reflects the variation of M and the output power.

C. Loss Analysis

There are two operational modes in the primary pad and the converter in a dynamic charging system: 1) standby and 2) charging. Normally, the period of standby is much longer than that of charging condition, and the exact value depends on actual vehicle flow. Thus, in dynamic WPT systems, the output power waveform looks like one or several nonperiodic pulses: when the EV is coming, the system will start up and the output power will reach the maximum value in a very short time; when the EV has passed, the output power will go down to zero and the system will stand by for a long time. Therefore, to such nonperiodic and variable load system, we think that the power loss comparison is more meaningful than efficiency to quantify the performance of the system.

TABLE III
DYNAMIC WPT CHARGING SYSTEM SPECIFICATION

Parameters	Values	Parameters	Values	Parameters	Values
L_{fl}	60 uH	L_a	60 uH	r_a	40 mohm
r_{Lfl}	20 mohm	r_{La}	20 mohm	R_a	10^4 ohm
C_{fl}	58.43 nF	C_a	116.8 nF	$M_{La\text{-}Lfl}$	45 uH
C_p	19.48 nF	C_{fa}	116.8 nF	U_{in}	320 V
L_1	260 uH	L_{fa}	30 uH	f	85 kHz
r_{L1}	60 mohm	r_{Lfa}	20 mohm	$\tan\theta$	0.0015
Z_{rmax}	30 ohm	$V_{forward}$	1.5 V		

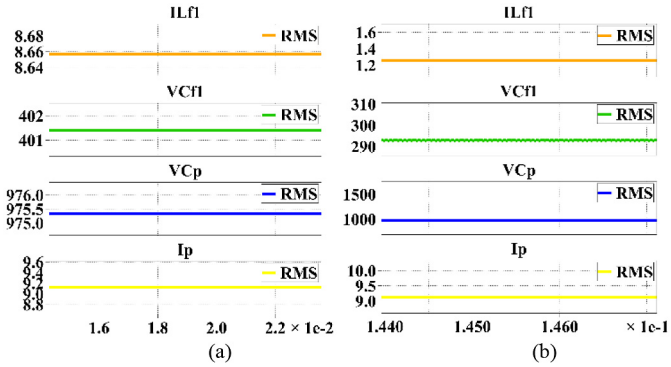

Fig. 11. RMS values in no-current-control method. (a) Charging condition. (b) Standby condition.

Assume that 30 square coils are placed side by side to compose a dynamic wireless charging primary pads and the side length of each coil is 1 m. Neglect the gap between the two adjacent coils, then the total dynamic wireless charging area length is 30 m. The loss comparison will be made between the multiple paralleled LCC with current regulation circuit for each RPCN network (shown in Fig. 8) and the conventional LCC topology without current limitation control method (shown in Fig. 3). The circuit parameters are shown in Table III.

In Table III, r is the wire resistor of the corresponding inductor, which is indicated by the subscript. V_{forward} is the forward voltage of the rectifier diode in current regulation circuit. $Z_{r\text{max}}$ is the equivalent reflected load value when the primary pad and the secondary coil are aligned; $\tan\theta$ is the loss angle of the capacitors. In this designing, WIMA MKP10 film capacitors are used and their loss angle is fixed at 1.5‰.

As shown in Fig. 6, there are five conditions in a power cycle. To simplify the results, only referring *point 1*, the maximum output power point is selected to make a loss analysis. The simulation was done using PLECS 3.5.

If there is no primary pad current limitation control method in the dynamic WPT system, the rms values of currents and voltages in the RPCN at two operational modes are shown in Fig. 11.

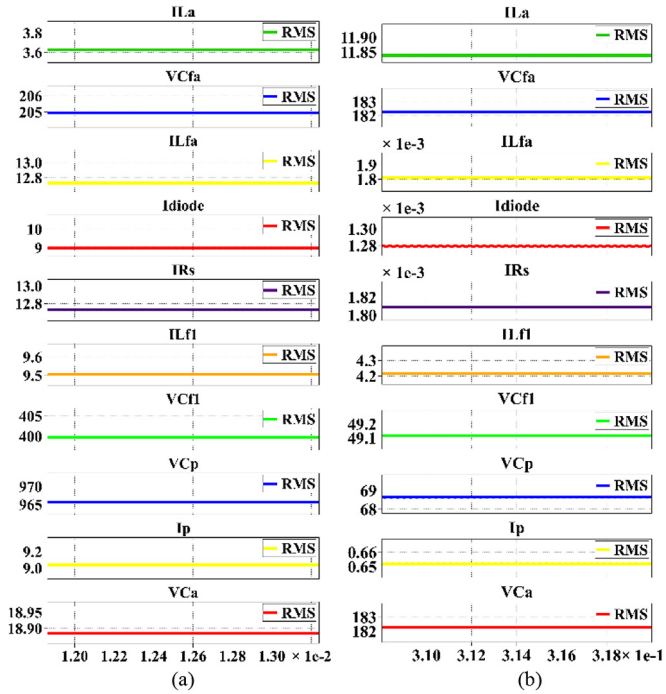

Fig. 12. RMS values in the primary pad current regulation circuit. (a) Charging condition. (b) Standby condition.

The capacitor loss could be calculated by

$$P_{c-\text{loss}} = \omega C V_c^2 \tan\theta \tag{14}$$

where $P_{c-\text{loss}}$ is the power loss of the capacitor; C is the capacitance; V_c is the voltage on the capacitor.

The total loss in this condition could be calculated as

$$P_{\text{loss1}} = I_{Lf1}^2 r_{Lf1} + I_{Lp}^2 r_{Lp} + \omega \tan\theta \left(C_{f1} V_{Cf1}^2 + C_p V_{Cp}^2\right). \tag{15}$$

From Table III, Fig. 11, and (15), the loss of working primary RPCN $P_{loss1-charging}$ is 28.95 W. The other 29 primary pads are working at standby condition, the calculated loss of each RPCN $P_{\text{loss1}-\text{standby}}$ is 24.56 W and the total standby loss is 29*$P_{\text{loss1}-\text{standby}}$ = 712.35 W. The total loss could be calculated as: 712.35 + 28.95 = 741.3 W.

If the primary pad current regulation circuit is used, the rms values of currents and voltages of the components at both standby and charging conditions are shown in Fig. 12.The total loss in this condition could be calculated as

$$\begin{aligned} P_{\text{loss2}} = {} & I_{La}^2 r_{La} + I_{Lfa}^2 r_{Lfa} + I_{Rs}^2 R_s + I_p^2 r_{L1} + I_{Lf1}^2 r_{Lf1} \\ & + \tan\theta \left(C_{fa} V_{Cfa}^2 + C_{f1} V_{Cf1}^2 + C_1 V_{C1}^2 + C_a V_{Ca}^2\right) \\ & + 2 V_{\text{forward}} I_{\text{diode}}. \end{aligned} \tag{16}$$

From Table III, Fig. 12, and (16), the loss of working primary RPCN $P_{\text{loss2}-\text{charging}}$ is 69.73 W. Other 29 primary pads are working at standby condition, calculated each RPCN's loss $P_{\text{loss2}-\text{standby}}$ is 9.9 W and the standby loss is 29*$P_{\text{loss2}-\text{standby}}$ = 287.1 W. The total loss could be calculated as: 287.1 + 69.73 = 356.83 W.

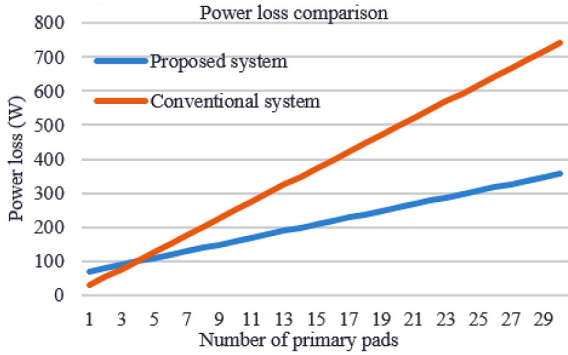

Fig. 13. Power loss comparison between two dynamic WPT systems.

From the numeric comparison, under the same circuit parameter condition, when the system operates at charging condition, the power loss in the circuit shown in Fig. 8 is two times more than that in Fig. 3, because the auxiliary current regulation circuit consumes a large amount of energy. However, as the primary pad currents are limited by the auxiliary circuit, the power loss in the circuit in Fig. 8 is only 1/3 of that in Fig. 3 at the standby condition. The calculation result showed that within 30 m charging area, the total loss in the proposed dynamic WPT system is only one half of that in conventional dynamic WPT system at the aligned condition. Fig. 13 is the power loss comparison between the two systems.

Fig. 13 shows that if the number of primary pads is more than 4, the proposed dynamic WPT system will be more efficient. It is also true that the more the primary pads, the lower the power loss. Please note that the magnetic loss and ac Litz wire loss is not include in this loss analysis; if these factors are considered, the loss in conventional dynamic WPT system will be much larger than the above calculated.

V. Experimental Validation

To validate the proposed circuit and the above analysis, a prototype of a dynamic WPT charging system was built with four DD pads in the primary side and the DDQ magnetic structure in the pickup side, compensated by double-sided LCC networks. The specifications of the prototype are given in Table IV. The physical setup is shown in Fig. 14. Four DD coils paralleled side by side to compose the primary pads array and are excited by a single inverter, and four primary coils in the auxiliary LCC RPCNs are closely coupled with the main power RPCNs correspondingly. Their self-inductance values are approximately identical with each other. Every auxiliary LCC primary coil and its corresponding main power freewheeling inductor are fixed on the two sides of a 5-mm thick plastic board. The controller is TMS320F28335 plus CPLD, and the details of the center control board are shown in Fig. 14. Two magnetic coupled gate drivers ADUM3223 are used to drive four SIC MOSFETs in the common inverter, and the details are also shown in Fig. 14. The resonant film capacitors are WIMA MKP10, and the loss angle is around 1.5‰ at 100 kHz. In the pickup side, a DD coil and a Q coil with the same number of turns are overlapped.

TABLE IV
DYNAMIC WPT CHARGING SYSTEM SPECIFICATION

Parameters	Values
U_{in}	70 VDC
L_{fk-1}, L_{fk}, L_{fk+1}, and L_{fk+2}	58.7 uH, 52.8 uH, 58.9 uH, 64.1 uH
C_{fk-1}, C_{fk}, C_{fk+1}, and C_{fk+2}	59.4 nF, 66.2 nF, 59.4 nF, 54.8 nF
L_{k-1}, L_k, L_{k+1}, and L_{k+2}	84.2 uH, 89.9 uH, 92.1 uH, 93.2uH
C_{k-1}, C_k, C_{k+1}, and C_{k+2}	137.6 nF, 94.7 nF, 105.8nF, 120.6 nF
$M_{ls\text{-}lk\text{-}1}$, $M_{ls\text{-}lk}$, $M_{ls\text{-}lk+1}$, and $M_{ls\text{-}lk+2}$	22.2 uH, 23.9 uH, 24.1 uH, 24.3 uH
$M_{lq\text{-}lk\text{-}1}$, $M_{lq\text{-}lk}$, $M_{lq\text{-}lk+1}$, and $M_{lq\text{-}lk+2}$	7.6 uH, 8.5 uH, 9.2 uH, 9.3 uH
r_{Lk-1}, r_{Lk}, r_{Lk+1}, and r_{Lk+2}	0.02 ohm

Parameters	Values	Parameters	Values
f	81.5 kHz	C_s	56.5 nF
L_s	93.8 uH	C_Q	184.2 nF
L_Q	47.7 uH	L_{sf}	31.5 uH,
DD coils size	300 mm*450 mm	L_{Qf}	28.7 uH
Distance	10 cm	C_{sf}	111.3 nF
Litz wire	AWG38*800	C_{Qf}	122.6 nF
R_s	40m ohm/ 3.2k ohm	R	35 ohm
Distance	7 cm	L_{fa}	31.2 uH

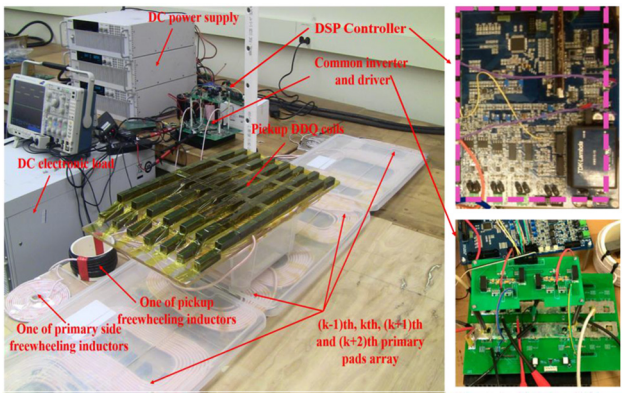

Fig. 14. Physical setup of the tested prototype.

Fig. 15 shows the experimental results of power distribution in the two primary LCC RPCNs. In Fig. 15(a), when the pickup coil was perfectly coupled with the kth primary coil, most of the input power was distributed to the kth LCC RPCN, whose input current was 2.63 A. The $(k+1)$th LCC RPCN input current was just 0.5 A. In Fig. 15(b), when the pickup coil was perfectly coupled with the $(k+1)$th primary coil, most of the input power was distributed to the $(k+1)$th LCC RPCN, whose input current-paralleled LCC RPCNs in the primary side could distribute input power automatically.

Fig. 16 is the primary coil current regulation experimental result. The top curve is the input voltage of an arbitrary LCC RPCN; the bottom curve is the current in C_{fa}; the middle curve is the primary coil current.

Initially, in t_1 period, the pickup coils and the primary coil were decoupled and the auxiliary LCC RPCN operates in open-circuit mode, the input current of the main power LCC RPCN and the primary coil current i_k are almost zero. With the secondary coils moving in t_2 period, the primary pad and the

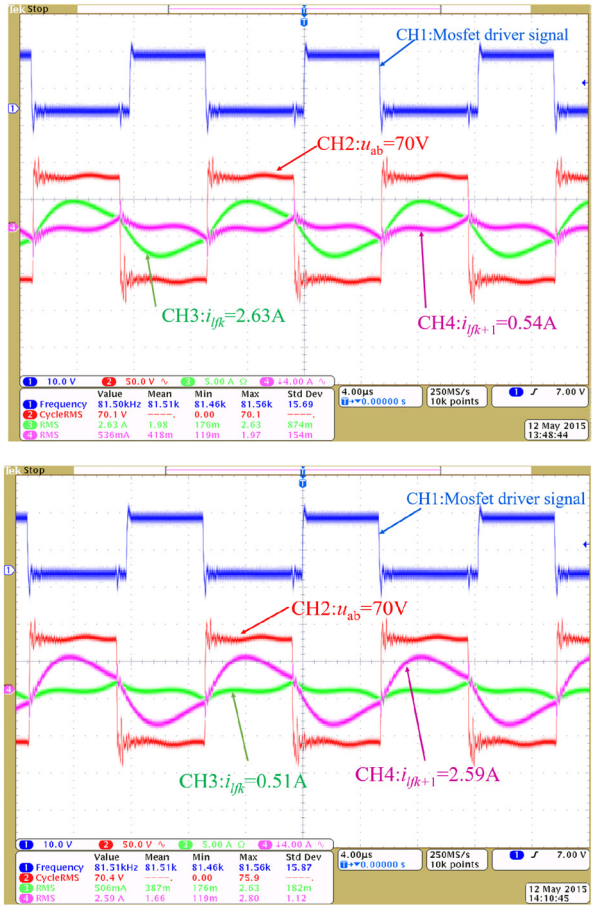

Fig. 15. Automatic power distribution validation. Top: kth coil coupled with pickup coils. Lower: $(k+1)$th coil coupled with pickup coils. CH1: inverter driver signal; CH2: common input voltage of two RPCNs; CH3: input current of kth RPCN; CH4: input current of $(k+1)$th RPCN.

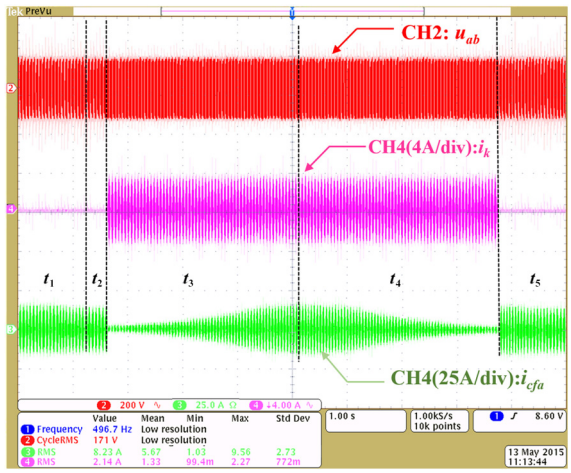

Fig. 16. Primary coil current regulation. CH2: top, common input voltage; CH3: bottom, the current in C_{fa}; CH4: middle, current in the kth coil.

receiver start to get partly coupled and i_{cfa} began to increase. At the beginning of t_3 period, as soon as i_{cfa} is larger than the preset value, the digital comparator will send a high-level signal to control the auxiliary LCC RPCN operating at short-circuit

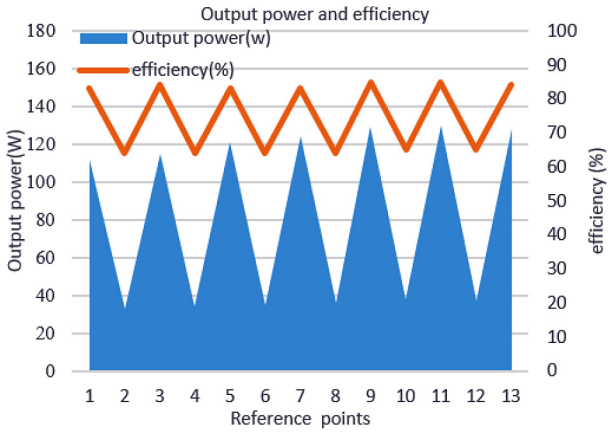

Fig. 17. Output power and efficiency curves.

mode, and i_k will achieve the maximum value in a short time. At the same time, i_{cfa} is decreased.

With the EV moving, both mutual inductance and i_{cfa} will reach the maximum amplitude at the end of t_3 period and will be decreased during t_4 period. At the beginning of t_5, the EV is moving away. As soon as i_{cfa} is smaller than the other preset value, the digital comparator will send a low-level signal to control the auxiliary LCC RPCN operating back to open-circuit mode and the primary coil current will decrease to a tiny value once more. Fig. 16 validated that the primary coil current regulation control method could perform well to regulate the primary coil current and improve system efficiency, and the experimental results matches the simulation as shown in Fig. 10. In addition, according to the waveform of the primary coil current, the response time of every switching is so short that the system has enough effective time for battery charging when the EV is moving.

The output power and efficiency curves are shown in Fig. 17. In Fig. 17, the *X*-axis is the reference points. There are 4 primary pads in the system, 3 power cycles, and 13 reference points (2 reference points are coincided). There are two *Y*-axis, one is the output power and the other is the system's total efficiency. From Fig. 17, the maximum output power points of the verification system are around 120 W, the minimum points are around 35 W; the maximum efficiency is 84% and the minimum efficiency is 65%. If there is no Q coil in the secondary, the minimum efficiency of the system will be zero.

In the experiment, the maximum value of R_s is only 3.2 k, which is much smaller than the simulation results. However, the performance of current regulation is roughly in agreement with the simulation results. Besides, there is a bit of oscillation in the input voltage waveforms in Fig. 15. These phenomena indicate that the system is not perfectly operated at constant resonant frequency. The reason is that a resonant system is very sensitive to large value of R_s. Therefore, the question of how to optimize the value of R_s is a meaningful future work.

VI. Conclusion

A novel circuit and its control method were proposed for the dynamic WPT system in this paper. The advantage of using multi-paralleled LCC RPCNs in the primary side is that all the subcompensation networks can be excited via a single inverter and the power between different networks can be distributed automatically depending on only the mutual inductance values. An auxiliary LCC network is proposed to limit the constant current in the primary coil, which significantly minimizes EMI and reduces the power loss of the system. The corresponding control strategy is also proposed to measure the variation in *M* and realized the exciting current in the primary pad regulation automatically.

Compared to powering several sectionalized transmitter coils or using one long track, the main benefits of the proposed system are: 1) there is only one power converter in the primary side, which minimizes the component cost; 2) no auxiliary position tracking detection circuits are needed, which significantly simplifies the control and improves system response speed; and 3) soft-switching with fixed constant resonant frequency in the inverter is realized during the whole power transfer process regardless of coupling variations or battery condition.

References

[1] H. G. Düsterwald, J. Günnewig, and P. Radtke, "DRIVE—The future of automotive power: Fuel cells perspective," *Fuel Cells*, vol. 7, no. 3, pp. 183–189, May 2007.

[2] J. Shin, "Design and implementation of shaped magnetic-resonance-based wireless power transfer system for roadway-powered moving electric vehicles," *IEEE Trans. Ind. Electron.*, vol. 61, no. 3, pp. 1179–1192, Mar. 2014.

[3] Q. Zhu, L. Wang, and C. Liao, "Compensate capacitor optimization for kilowatt-level magnetically resonant wireless charging system," *IEEE Trans. Ind. Electron.*, vol. 61, no. 12, pp. 6758–6768, Dec. 2014.

[4] S. Li and C. C. Mi, "Wireless power transfer for electric vehicle applications," *IEEE Trans. Emerg. Sel. Topics Power Electron.*, vol. 3, no. 1, pp. 4–17, Mar. 2015.

[5] C.-H. Ou, H. Liang, and W. Zhuang, "Investigating wireless charging and mobility of electric vehicles on electricity market," *IEEE Trans. Ind. Electron.*, vol. 62, no. 5, pp. 3123–3133, May 2015.

[6] I.-S. Suh and J. Kim, "Electric vehicle on-road dynamic charging system with wireless power transfer technology," in *Proc. IEEE Int. Elect. Mach. Drives Conf. (IEMDC)*, May 12–15, 2013, pp. 234–240.

[7] T. Theodoropoulos *et al.*, "Impact of dynamic EV wireless charging on the grid," in *Proc. IEEE Int. Elect. Veh. Conf. (IEVC)*, Dec. 17–19, 2014, pp. 1–7.

[8] G. A. J. Elliot, J. T. Boys, and G. A. Covic, "A design methodology for flat pick-up ICPT systems," in *Proc. IEEE 1st Conf. Ind. Electron. Appl.*, May 24–26, 2006, pp. 1–7.

[9] S. Choi, J. Huh, W. Y. Lee, S. W. Lee, and C. T. Rim, "New cross-segmented power supply rails for roadway-powered electric vehicles," *IEEE Trans. Power Electron.*, vol. 28, no. 12, pp. 5832–5841, Dec. 2013.

[10] B.-M. Song, R. Kratz, and S. Gurol, "Contactless inductive power pickup system for Maglev applications," in *Proc. 37th IEEE IAS Annu. Meeting*, Oct. 13–18, 2002, vol. 3, pp. 1586–1591.

[11] J. Huh, W. Lee, G.-H. Cho, B. Lee, and C.-T. Rim, "Characterization of novel inductive power transfer systems for on-line electric vehicles," in *Proc. 26th Annu. IEEE Appl. Power Electron. Conf. Expo. (APEC)*, Mar. 6–11, 2011, pp. 1975–1979.

[12] J. Kim, D.-H. Kim, and Y.-J. Park, "Analysis of capacitive impedance matching networks for simultaneous wireless power transfer to multiple devices," *IEEE Trans. Ind. Electron.*, vol. 62, no. 5, pp. 2807–2813, May 2015.

[13] O. C. Onar, J. M. Miller, S. L. Campbell, C. Coomer, C. P. White, and L. E. Seiber, "A novel wireless power transfer for in-motion EV/PHEV charging," in *Proc. 28th Annu. IEEE Appl. Power Electron. Conf. Expo. (APEC)*, Mar. 17–21, 2013, pp. 3073–3080.

[14] G. A. Covic and J. T. Boys, "Modern trends in inductive power transfer for transportation applications," *IEEE Trans. Emerg. Sel. Topics Power Electron.*, vol. 1, no. 1, pp. 28–41, Mar. 2013.

[15] J. M. Miller *et al.*, "Demonstrating dynamic wireless charging of an electric vehicle: The benefit of electrochemical capacitor smoothing," *IEEE Power Electron. Mag.*, vol. 1, no. 1, pp. 12–24, Mar. 2014.

[16] G. R. Nagendra, J. T. Boys, G. A. Covic, B. S. Riar, and A. Sondhi, "Design of a double coupled IPT EV highway," in *Proc. 39th Annu. Conf. IEEE Ind. Electron. Soc. (IECON'13)*, Nov. 10–13, 2013, pp. 4606–4611.
[17] K. Lee, Z. Pantic, and S. M. Lukic, "Reflexive field containment in dynamic inductive power transfer systems," *IEEE Trans. Power Electron.*, vol. 29, no. 9, pp. 4592–4602, Sep. 2014.
[18] A. P. Hu, J. T. Boys, and G. A. Covic, "ZVS frequency analysis of a current-fed resonant converter," in *Proc. 7th IEEE Int. Power Electron. Congr. (CIEP'00)*, 2000, pp. 217–221.
[19] H. H. Wu, A. Gilchrist, K. D. Sealy, and D. Bronson, "A high efficiency 5 kW inductive charger for EVs using dual side control," *IEEE Trans. Ind. Informat.*, vol. 8, no. 3, pp. 585–595, Aug. 2012.
[20] C. S. Tang, Y. Sun, Y. G. Su, S. K. Nguang, and A. P. Hu, "Determining multiple steady-state ZCS operating points of a switch-mode contactless power transfer system," *IEEE Trans. Power Electron.*, vol. 24, no. 2, pp. 416–425, Feb. 2009.
[21] B. Sharp and H. Wu, "Asymmetrical voltage-cancellation control for LCL resonant converters in inductive power transfer systems," in *Proc. 27th Annu. IEEE Appl. Power Electron. Conf. Expo. (APEC'12)*, Feb. 5–9, 2012, pp. 661–666.
[22] P. Si, A. P. Hu, S. Malpas, and D. Budgett, "A frequency control method for regulating wireless power to implantable devices," *IEEE Trans. Biomed. Circuits Syst.*, vol. 2, no. 1, pp. 22–29, Mar. 2008.
[23] M. Budhia, J. T. Boys, G. A. Covic, and C.-Y. Huang, "Development of a single-sided flux magnetic coupler for electric vehicle IPT charging systems," *IEEE Trans. Ind. Electron.*, vol. 60, no. 1, pp. 318–328, Jan. 2013.
[24] J. T. Boys, G. A. Covic, and A. W. Green, "Stability and control of inductively coupled power transfer systems," *Proc. Inst. Elect. Eng.—Elect. Power Appl.*, vol. 147, no. 1, pp. 37–43, Jan. 2000.

Shijie Zhou received the Ph.D. degree in control theory and control engineering from Chongqing University, Chongqing, China, in 2012.

He is currently a Postdoctoral Researcher with the Department of Electrical and Computer Engineering, College of Engineering, University of Michigan, Dearborn, MI, USA. His research interests include power electronics and wireless power transfer.

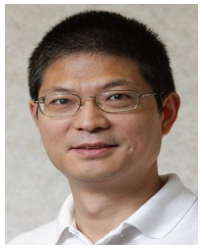

Chunting Chris Mi (S'00–A'01–M'01–SM'03–F'12) received the B.S.E.E. and M.S.E.E. degrees in electrical engineering from Northwestern Polytechnic University, Xi'an, China, and the Ph.D. degree in electrical engineering from the University of Toronto, Toronto, ON, Canada.

He is a Professor and Chair of Electrical and Computer Engineering, San Diego State University, San Diego, CA, USA. Previously, he was a Professor with the University of Michigan, Dearborn, MI, USA. Prior to joining the University of Michigan in 2001, he was with General Electric Company, Peterborough, ON, Canada. He has conducted extensive research and has published more than 100 journal papers. His research interests include electric drives, power electronics, electric machines, renewable energy systems, and electrical and hybrid vehicles.

Dr. Mi is an Area Editor of the IEEE TRANSACTIONS ON VEHICULAR TECHNOLOGY.